PHYSICAL REVIEW B **101**, 165410 (2020)

Strong electromagnetic coupling in dimers of topological-insulator nanoparticles and quantum emitters

G. D. Chatzidakis and V. Yannopapas*
Department of Physics, National Technical University of Athens, GR-157 80 Athens, Greece

(Received 17 April 2019; revised manuscript received 14 March 2020; accepted 17 March 2020; published 8 April 2020)

In this work, we theoretically investigate the optical properties of a topological-insulator nanoparticle–quantum emitter dimer interacting in the strong-coupling regime. The calculations are based on a recently developed semianalytical technique based on a multiple-scattering polaritonic-operator formalism in conjunction with an electromagnetic coupled dipole method. We calculate the light spectrum of the above dimer and report the emergence of a mode that stems from the coupling of the surface topological particle polariton of the topological insulator with the resonance state of the quantum emitter.

DOI: 10.1103/PhysRevB.101.165410

I. INTRODUCTION

In condensed-matter physics, classifying distinct phases of matter has been traditionally understood in terms of the spontaneous breaking of underlying symmetries [1] of the relevant systems. A notable exception regarding this classification paradigm is the quantum spin Hall effect [2] introducing the notion of topological order [3,4], i.e., that these states of matter do not spontaneously break any symmetries yet define a topological phase in the sense that certain fundamental properties of such states remain unaffected with respect to smooth changes in material parameters. Recently, a new class of materials has emerged, namely, that of topological insulators (TIs) [5], that has attracted a lot of attention in the field of solid-state physics [6]. Topological insulators are electronic materials that have a bulk band gap like an ordinary insulator but have protected conducting states on their edge or surface. Such states are possible due to the combination of spin-orbit interactions and time-reversal symmetry [7,8]. They have been experimentally observed in mercury telluride quantum wells [9,10], bismuth antimony alloys [11,12], and $\mathrm{Bi_2Te_3}$ and $\mathrm{Bi_2Se_3}$ bulk crystals [13–16], while further studies have been performed in spherical [17–19] and cylindrical [20–22] geometries as well as bulk TIs terminated at an arbitrary crystal face [23] and thin films [24].

Recently, the impact of such topologically protected (surface) states in the optical properties of topological insulator nanoparticles (TINPs) was investigated [25], illustrating that, under the influence of light, a single electron in such a state creates a surface charge density similar to a plasmon in a metallic nanoparticle. Furthermore, such an electron can act as a screening layer, effectively suppressing absorption inside the particle, and can couple phonons and light, giving rise to a previously unreported topological particle polariton mode. In the present work, we theoretically investigate the behavior of this surface topological particle (SToP) mode in the case where the TINP interacts strongly with a single quantum emitter (QE) by means of calculation of the light spectrum of the system. We find, in particular, that the SToP mode couples strongly with the resonance of the QE, giving rise to a hybrid mode, the signal output of which, as well as its spectral location, can be primarily tuned by controlling the TINP size. This result could prove useful in enhanced light-matter interactions in the terahertz range where the systems under study are QE-TINP arrays (for instance, binary chains) and calls for more investigation. The calculations were performed by implementing a previously developed technique [26], based on a multiple-scattering polaritonic-operator formalism [27,28] in conjunction with an electromagnetic coupled dipole method that enables the study of hybrid collections of quantum emitters (atoms, molecules, and quantum dots) with nanoparticles (NPs). As a result, it can be further utilized in future studies of collections comprised of *many* QE-TINP dimers.

II. THEORY

In this section the two main components of the method analytically presented in Ref. [26] are outlined. During the first step of the following method, a collection of nanoparticles is initially assumed to be embedded inside a material, while the quantum emitters are assumed to be inserted *a posteriori*. This initial “bare” system (NPs + dielectric) is described in terms of the coupled dipole approximation (CDA) wherein the nanoparticles are modeled as point dipoles and quantum emitters are modeled as fictitious point dipoles with zero polarizability. This allows for the calculation of the (local) electric field $\mathbf{E}(\mathbf{r},\omega)$, which excites a fictitious dipole located at $\mathbf{r}$ as the sum of the directly incident field on the (fictitious) dipole plus the field scattered off all other dipoles (corresponding to the NPs of the bare system) incoming to the specific dipole. Via the same scheme, one may calculate the electromagnetic (EM) Green’s tensor dyadic $\mathbf{G}(\mathbf{r},\mathbf{r}';\omega)$, where $\mathbf{r}$ and $\mathbf{r}'$ are positions of the above fictitious dipoles both for $\mathbf{r}=\mathbf{r}'$ and

---

*Corresponding author: vyannop@mail.ntua.gr

$\mathbf{r} \neq \mathbf{r}'$. Namely, $\mathbf{G}(\mathbf{r}, \mathbf{r}'; \omega)$ of a collection of M NPs (where $\mathbf{r}$ and $\mathbf{r}'$ are two position vectors in space) is calculated in the following manner. In order to calculate $\mathbf{G}$ for $\mathbf{r} = \mathbf{r}'$, $M + 1$ dipoles are constructed, where the first M correspond to the NPs of the above collection (with polarizabilities as described further below) while the last one corresponds to a fictitious dipole (at $\mathbf{r} = \mathbf{r}'$) with polarizability set to zero. Similarly, in order to calculate $\mathbf{G}$ for $\mathbf{r} \neq \mathbf{r}'$, $M + 2$ dipoles are constructed and the last two polarizabilities are set to zero, corresponding to two fictitious dipoles (located at $\mathbf{r}$ and $\mathbf{r}'$).

Within the CDA, one may calculate the classical EM Green's tensor dyadic between the ith and jth dipoles, $\mathbf{G}_{ij}(\omega)[\equiv \mathbf{G}(\mathbf{r}_i, \mathbf{r}_j; \omega)]$, for a finite collection of M nanoparticles (modeled as point dipoles) embedded in a material of relative dielectric permittivity ϵ_d via the following linear system of $3M$ equations [29]:

$$\sum_{k}^{M} \left[\delta_{ik} - \frac{\omega^2}{c^2} \alpha_k(\omega) \cdot \mathbf{G}^0_{ik}(\omega) \right] \cdot \mathbf{G}_{kj}(\omega) = \mathbf{G}^0_{ij}(\omega). \qquad (1)$$

Here, $\mathbf{G}^0_{ij} = \frac{e^{ikr_{ij}}}{4\pi r_{ij}} [(1 + \frac{ikr_{ij}-1}{k^2 r^2_{ij}}) \cdot \mathbf{1}_3 + \frac{3-3ikr_{ij}-k^2r^2_{ij}}{k^2 r^2_{ij}} \cdot (\hat{\mathbf{r}}_{ij} \otimes \hat{\mathbf{r}}_{ij})]$ is the (homogeneous) free- space Green's tensor ($k^2 = \frac{\omega^2}{c^2}$), and α_k is the polarizability tensor of the kth nanoparticle. Furthermore, using the scheme involving the fictitious dipoles mentioned in the beginning of this section, one may also evaluate $\mathbf{G}_{ij}(\omega)$ at the positions of the quantum emitters (to be inserted). Equation (1) is solved by employing a numerical solver such as a conjugate gradient method.

In our work, an accurate formula for the polarizability was chosen so as to account for the radiation-reaction effect [30–32]:

$$\alpha(\omega) = \frac{\alpha^0(\omega)}{1 - \frac{i\alpha^0(\omega)\omega^3\sqrt{\epsilon_d}}{6\pi c^3}}. \qquad (2)$$

Here, $\alpha^0(\omega)$ is the bare polarizability, given by the Clausius-Mossoti relation, typical for small spherical nanoparticles of radius S, with relative dielectric permittivity ϵ_m embedded in a material of relative dielectric permittivity ϵ_d:

$$\alpha^0(\omega) = 4\pi\epsilon_d S^3 \frac{\epsilon_m(\omega) - \epsilon_d}{\epsilon_m(\omega) + 2\epsilon_d}. \qquad (3)$$

Given this finite collection of M nanoparticles, one may solve the light-scattering problem within the coupled dipole method. Specifically, if the above collection is embedded in a material of relative dielectric permittivity ϵ_d and impinged by an incident field $\mathbf{E}^{\mathrm{inc}}$, the (local) electric field $\mathbf{E}_i$ that excites the ith dipole of the collection can be obtained through [33,34]

$$\mathbf{E}_i(\omega) = \left(\mathbf{E}^{\mathrm{inc}}_i(\omega) + k^2 \sum_{j \neq i}^{M} \mathbf{G}^0_{ij}(\omega) \cdot \alpha_j(\omega) \cdot \mathbf{E}_j(\omega) \right). \qquad (4)$$

Within the CDA, the dipole moment of each NP ($\mathbf{P}_i = \alpha_i \cdot \mathbf{E}_i$) is initially calculated via the following system of $3M$ equations [33]:

$$\sum_{j}^{M} \left[\delta_{ij} - k^2 \alpha_i(\omega) \cdot \mathbf{G}^0_{ij}(\omega) \right] \cdot \mathbf{P}_j(\omega) = \alpha_i(\omega) \cdot \mathbf{E}^{\mathrm{inc}}_i(\omega). \qquad (5)$$

Here, M is the number of the NPs and $\mathbf{E}^{\mathrm{inc}}_i$ is the incident field at the position of the ith nanoparticle of the bare collection. One can then calculate quantities such as the absorption, scattering, and extinction cross sections of the collection (see Sec. III).

Having calculated the dipole moments of the nanoparticles, one can afterwards evaluate the (local) field at the position of each fictitious dipole of a collection of $N + M$ dipoles where N corresponds to fictitious ones with zero polarizability (N quantum emitters to be inserted) and M corresponds to the nanoparticles of the bare system, again via Eq. (4):

$$\mathbf{E}_i(\omega) = \mathbf{E}^{\mathrm{inc}}_i(\omega) + \sum_{j}^{M} k^2 \mathbf{G}^0_{ij}(\omega) \cdot \mathbf{P}_j(\omega). \qquad (6)$$

Here, however, i always concerns the ith fictitious dipole while j runs through the *entire* collection of the M dipoles corresponding to the nanoparticles of the bare system.

Afterwards, the ensemble of quantum emitters may be inserted into the bare system via the second component of our method, i.e., the multiple-scattering formalism. Here, one typically starts with the following diagonalized Hamiltonian stemming from a macroscopic QED formalism [35,36]:

$$\mathcal{H} = \int d^3\mathbf{r} \int_0^\infty d\omega \hbar\omega \hat{\mathbf{f}}^\dagger(\mathbf{r}, \omega; t) \cdot \hat{\mathbf{f}}(\mathbf{r}, \omega; t) + \sum_{n=1}^{N} \frac{\hbar}{2} \Omega_n \hat{\sigma}^z_n(t) - \sum_{n=1}^{N} [\hat{\sigma}^+_n(t) + \hat{\sigma}^-_n(t)] \mathbf{P}_n \cdot (\hat{\mathbf{F}}^{(+)}(\mathbf{r}; t) + \hat{\mathbf{F}}^{(-)}(\mathbf{r}; t)). \qquad (7)$$

In Eq. (7) all EM information regarding the nanoparticles is remapped in the dyadic Green's function of the bare system (NPs and surrounding dielectric) $\mathbf{G}(\mathbf{r}, \mathbf{r}'; \omega)$, as one may observe in the expression of the electric field operator,

$$\hat{\mathbf{F}}^{(+)}(\mathbf{r}, \omega; t) = i \sqrt{\frac{\hbar}{\pi\epsilon_0}} \int_0^\infty d\omega \frac{\omega^2}{c^2} \int d^3\mathbf{r}' \sqrt{\mathrm{Im}\,[\epsilon_m(\mathbf{r}', \omega)]} \times \mathbf{G}(\mathbf{r}, \mathbf{r}', \omega) \cdot \hat{\mathbf{f}}(\mathbf{r}', \omega; t), \qquad (8)$$

where $\epsilon_m(\mathbf{r}, \omega)$ is the complex dielectric function of the nanoparticles. $\mathbf{G}(\mathbf{r}, \mathbf{r}'; \omega)$ can be determined via Eq. (1) in the context of CDA. The first term of the Hamiltonian involves the polaritonic vector field operators $\hat{f}(\mathbf{r}, \omega; t)$, and represents the elementary excitations of the light-matter system. The quantum emitters are introduced as point dipoles with dipole moment $\mathbf{P}_n$ and natural frequency Ω_n (assumed complex $\Omega_n = \omega_0 - i\gamma_{\mathrm{QE}}/2$ to account for internal nonradiative decay rate γ_{QE}) through the Pauli operators $\hat{\sigma}_n$ in the second term of the Hamiltonian. The third term represents the coupling between the ensemble of quantum emitters and the bare system (NPs and dielectric).

Following the procedure introduced in Ref. [27], one may obtain the electric field operators by means of a multiple-scattering problem. Specifically, by performing a Laplace transform in the Heisenberg equations of motion, and then tracing out the fermionic operators ($\hat{\sigma}$), one may obtain a Lippman-Schwinger equation for the field operator $\hat{\mathbf{F}}$, where the quantum emitters appear as point scatterers and quantum source operators. In the process, the low-excitation-regime hypothesis is assumed in order to approximate ($\hat{\sigma}$) as bosonic, while the electric field operators are determined via multiple-scattering techniques. The process sketched above, and described in more detail in Ref. [28], allows for the definition of a "dressed" dyadic Green's function, the N-scattering Green's tensor $\mathbf{G}^{(N)}_{\text{source}}(\mathbf{r}, \mathbf{r}_n; \omega)$ associated with the fluorescence of the N quantum emitters of the ensemble. $\mathbf{G}^{(N)}_{\text{source}}(\mathbf{r}, \mathbf{r}_n; \omega)$ can be used to describe the full propagation from the n_0th QE to the detector (placed at $\mathbf{r} = \mathbf{R}$) via its corresponding light spectrum,

$$S_{n_0}(\mathbf{R}, \omega) = \sum_{n}^{N} \left| \frac{\omega^2}{\epsilon_0 c^2} \mathbf{G}^{(N)}_{\text{source}}(\mathbf{R}, \mathbf{r}_n; \omega) \cdot \mathbf{P}_n \right|^2 \times \left(\frac{\delta_{n,n_0}}{|\omega - \Omega_n|^2} + \frac{1 - \delta_{n,n_0}}{|\omega + \Omega_n|^2} + \frac{\delta_{n,n_0}}{|\omega + \Omega_n|^2} \right), \tag{9}$$

then summed incoherently over n_0 in order to obtain the light spectrum stemming from all quantum emitters measured at the position of the detector,

$$S(\mathbf{R}, \omega) = \sum_{n_0}^{N} |b_{n_0}|^2 S_{n_0}(\mathbf{R}, \omega), \tag{10}$$

with $b_{n_0} = \mathbf{P}_{n_0} \cdot \mathbf{E}_0(\mathbf{r}_{n_0}, \omega)$. $\mathbf{E}_0$ is the (classical) electric field amplitude of an incident plane wave scattered by the nanoparticles, incoming to the positions of the QEs. It can be calculated in the context of CDA, via Eq. (6), for an incident plane wave $\mathbf{E}_0^{\text{inc}} = E_0^{\text{inc}} e^{ik\cdot r}$ that excites the QE-NP collection.

III. RESULTS AND DISCUSSION

The spherical insulator nanoparticle (INP) under study (see Fig. 1) is made of Bi_2Se_3 in which case the bulk dielectric function is modeled by

$$\epsilon_{\text{inp}}(\omega) = \sum_{j=\alpha,\beta,f} \frac{\omega_{pj}^2}{\omega_{0j}^2 - \omega^2 - i\gamma_j \omega} \tag{11}$$

and includes contributions from α and β transverse phonons, and free charge carriers (f) arising from the bulk defects. The parameters for the three terms present in Eq. (11) are taken from a fit to experimental data [37] on bulk Bi_2Se_3. In Ref. [25] the surface states were found using a low-energy Hamiltonian valid close to the Dirac point [22,38]. Specifically, time-dependent perturbation theory was employed in the analytical model of a spherical TINP [22] which, for small radii, yields a discretized Dirac cone on a spherical surface. The effect of the topologically protected surface states is then reflected on the dielectric function of Eq. (11) via inclusion of a TINP radius-dependent term δ_R [25],

$$\delta_R = \frac{e^2}{6\pi\epsilon_0} \left(\frac{1}{2A - \hbar\omega R} + \frac{1}{2A + \hbar\omega R} \right). \tag{12}$$

Here, R is the TINP radius, ω is the angular frequency of the incident light, and $A = 0.3$ eV nm is a constant obtained from density functional theory calculations [38], related to the equally spaced surface states of the TINP that stem from spin-orbit coupling (see the supplemental material of Ref. [25]).

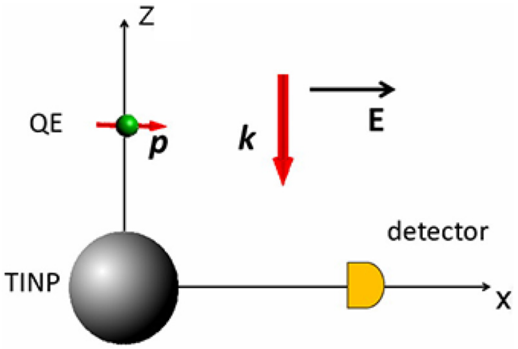

FIG. 1. Calculation (of light spectrum) setup: A Bi_2Se_3 TINP-QE dimer is illuminated by a normally incident field ($\mathbf{k} \parallel \mathbf{z}$). The corresponding electric field is polarized along the x axis while the dipole moment of the QE is assumed to be parallel with the former. The detector is placed at a theoretically infinite distance (practically at a very large distance) so as to capture only the far-field components of light. The absorption cross section (see main text) is calculated for the TINP in the absence of QE.

Introducing this term results in the modified dielectric function for a TINP,

$$\epsilon_{\text{tinp}} = \epsilon_{\text{inp}} + \delta_R. \tag{13}$$

In Fig. 2 we present results of the absorption cross section of a single Bi_2Se_3 TINP (which for the following calculations is modeled as a point dipole) of varying radius embedded in vacuum ($\epsilon_d = 1$) in order to probe the two main features reported in Ref. [25], namely, the SToP mode and the point of zero absorption, via

$$C_{\text{abs}} = \frac{4\pi k}{|E_0^{\text{inc}}|^2} \sum_{i=1}^{M} \left[\text{Im}(\mathbf{P}_i \cdot \mathbf{E}_i^*) - \frac{2}{3} k^3 |\mathbf{P}_i| \right], \tag{14}$$

where E_i and P_i are the local electric field at the position of each point dipole and its corresponding dipole moment, both calculated within the CDA. The TINP is illuminated by a normally incident plane wave ($\mathbf{k} \parallel \mathbf{z}$),

$$\mathbf{E}_0^{\text{inc}} = E_0^{\text{inc}} e^{-ik\cdot z} \hat{x}. \tag{15}$$

For TINP radii in the range 40–90 nm, the SToP mode lies in the frequency range between the Bi_2Se_3 localized surface plasmon-polariton (LSPP) mode located at 1 THz and the β phonon located at 3.72 THz. For the above range, aside from the presence of the SToP mode, it is evident that the zero in absorption is present at frequencies obeying $2A = \hbar\omega R$ [25]. Of note is the fact that the SToP mode diminishes with increasing particle size as the former approaches the frequency of the α phonon of Bi_2Se_3 located at 2 THz, hinting at one of the conclusions of Ref. [25], namely, that the mode arises due to the interaction of the electrons in the surface states with the bulk α phonon. For a TINP size of $R \approx 73.8$ nm, the SToP mode is located directly at the location of the α phonon, thus nearly fully suppressed, yielding an absorption cross section that differs from the corresponding of an ordinary insulator nanoparticle only by the zero in absorption (Fig. 3).

In all the following we calculate the light spectra (in arbitrary units) of TINP-QE hybrid systems with respect to incident light angular frequency (ω) as described by Eq. (10)

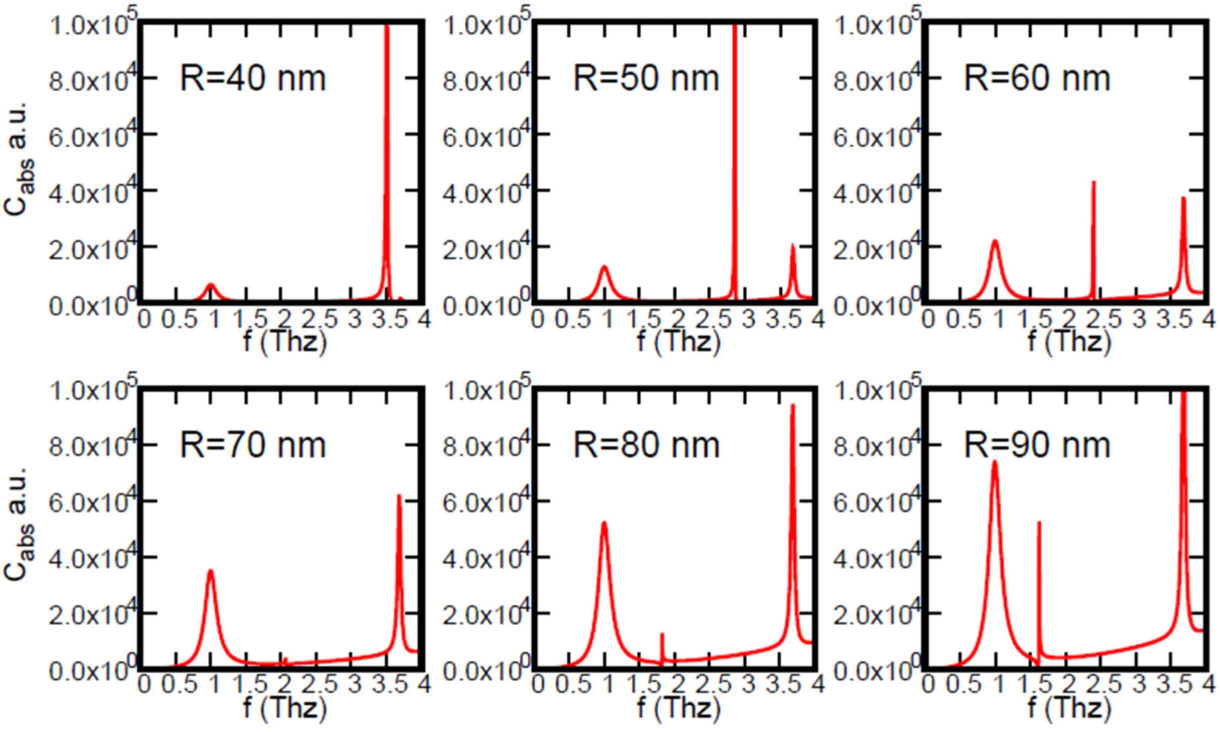

FIG. 2. Absorption cross section of a single Bi_2Se_3 TINP embedded in vacuum of varying radius as discussed in the main text. The key features are the emergence of the SToP mode accompanied by a zero in absorption. With increasing TINP radius, bulk effects become more prominent as reflected in the progressively stronger LSPP and β-phonon peaks. The SToP mode peak is significantly weaker in the vicinity of the α phonon, hinting at the coupling of the surface topological plasmon with the former.

and the method discussed in the previous section, wherein the QE transition angular frequency (ω_0) is parametrically varied. The computational setup we have assumed is shown in Fig. 1. The light spectra have been calculated via a programming code implementing the above method using a discretization of 201 steps for the frequency domain, corresponding to a mesh of 201×201 frequencies. The results in all subsequent figures are presented in terms of incident light frequency (f) and QE transition frequency (f_0). For the first set of calculations we choose a TINP of $R = 50$ nm. Namely, we calculate the light spectrum of a hybrid nanostructure comprised of a single TINP interacting with a two-level QE placed 1 nm above it to ensure strong interaction between the TINP and QE. The system, as with the previous calculations, is assumed to be embedded in vacuum and illuminated by a normally incident plane wave with an electric field polarized along the x axis. The transition dipole moment of the quantum emitter is set to $\mathbf{P} = 0.2\ e$ nm, parallel with the electric field. The light

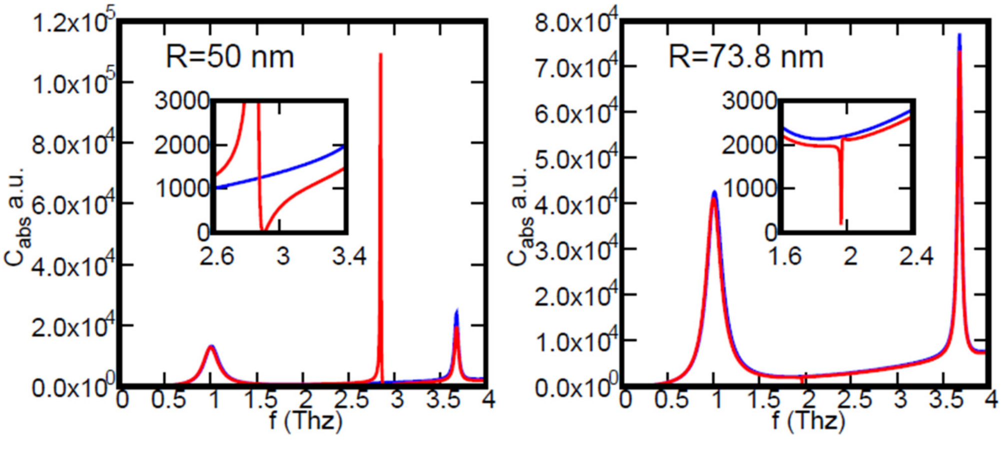

FIG. 3. Absorption cross section of a single Bi_2Se_3 TINP (red) embedded in vacuum juxtaposed with the absorption cross section of an ordinary INP (blue) of the same radius. For $R = 50$ nm (left), the zero in absorption is accompanied by the (prominent) SToP mode. For $R = 73.8$ nm (right), the SToP mode is tuned to the frequency of the bulk α phonon, rendering it nearly nonexistent with the zero in absorption remaining the only discernible difference with the absorption cross section of an ordinary insulator nanoparticle of the same radius.

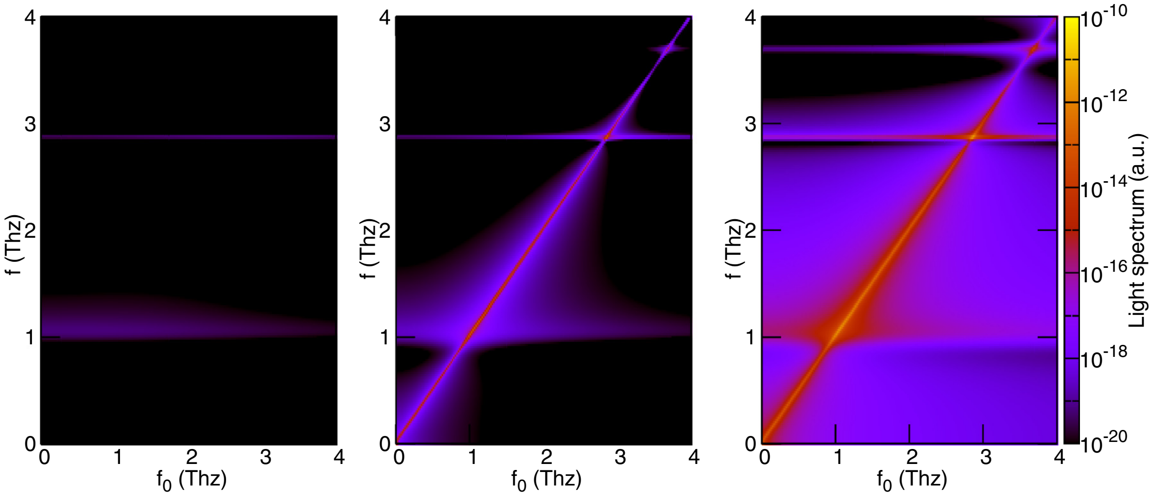

FIG. 4. Light spectra of the hybrid system under study for the case for $\gamma_{\text{qe}} = 15$ meV (left) and for $\gamma_{\text{qe}} = 0.8$ μeV (middle and right). It can be seen that the QE resonance couples with the SToP polariton, giving rise to a previously unreported mode. The right-hand panel is the same as the middle one, but for a five-times-larger value of the dipole moment, in order to clearly discern the characteristics of the coupling.

spectrum is obtained at (theoretically) infinite distance along the x axis (practically at a large distance) so as to capture only the far-field components of light. Figure 4 illustrates the importance of the value of the internal nonradiative decay rate γ_{qe} to the coupling of the SToP polariton with the QE resonance. Corresponding light spectra are presented respectively for the case of a QE with a slow decay rate, $\gamma_{\text{qe}} = 15$ meV (e.g., an organic molecule) and a fast decay rate, $\gamma_{\text{qe}} = 0.8$ μeV (e.g., a quantum dot [39,40]). For the slow decay rate (left-hand panel of Fig. 4), the light spectrum is almost featureless. For the fast decay rate (middle and right-hand panels of Fig. 4), it is evident that there is an avoided crossing area in the region of the SToP mode corresponding to the coupling between the QE resonance and the surface topological particle polariton, giving rise to a novel mode. The mode, as can be seen in Fig. 4 (right-hand panel) wherein the coupling strength was tuned at fivefold to accurately capture the features of the coupling, presents a bottleneck below the avoided crossing area that stems from the spectral vicinity of the SToP mode with the zero in the absorption cross section of the TINP (Fig. 2). We must stress here that assuming a QE with fast decay rate ($\gamma_{\text{qe}} = 0.8$ μeV) means considering the exciton resonance of a quantum dot which might reach the size of 10 nm. In that case, our formalism, which treats QEs as point objects, cannot account for possible size effects that may occur and can be taken into account by classical EM treatments of the excitons [41–43]. However, finer quantum phenomena such as superradiance or quenching of fluorescence cannot be captured unless the quantum mechanics of the QE-NP hybrid comes into play [44–48].

In all the following calculations we assume a TINP-QE system with $\gamma_{\text{qe}} = 0.8$ μeV embedded in vacuum ($\epsilon_d = 1$)

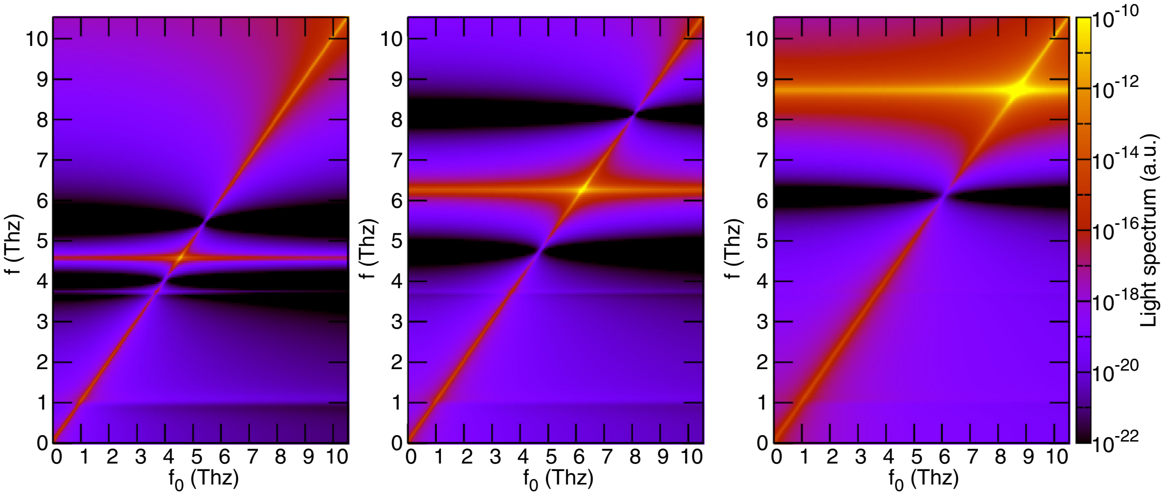

FIG. 5. Light spectra of the hybrid system under study for TINP radius $R = 30$ nm (left), $R = 20$ nm (middle), and $R = 10$ nm (right). The coupling between the SToP polariton and the QE resonance grows stronger and blueshifts as the TINP size decreases. The output signal of the coupling (middle of the avoided crossing area) as well as its spectral location can be tuned simply by controlling the TINP size (in all cases the system is assumed to be embedded in air).

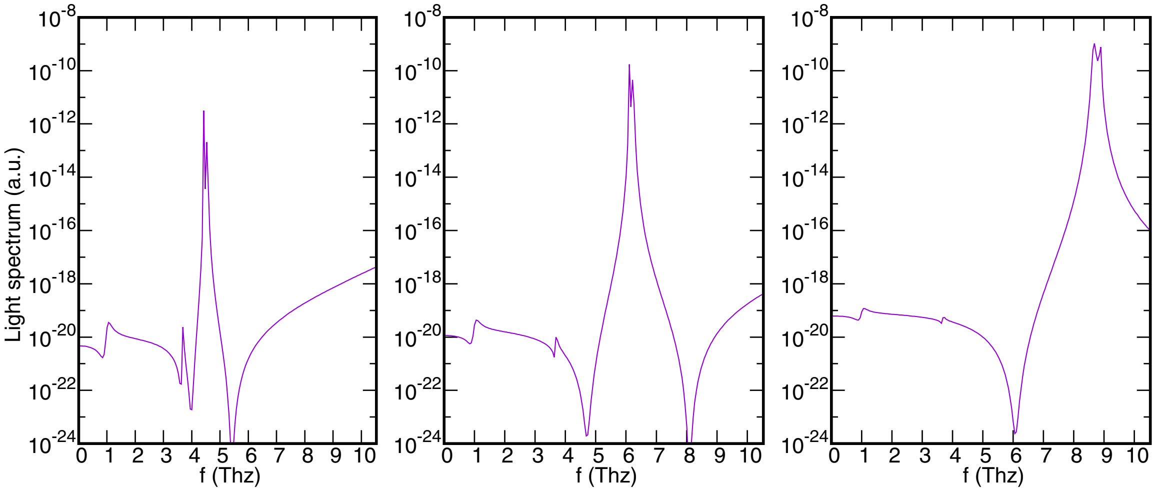

FIG. 6. Line plots of the light spectra of the hybrid system under study for a TINP radius $R = 30$ nm (left), $R = 20$ nm (middle), and $R = 10$ nm (right), with respect to incident light frequency (f) wherein the quantum emitter resonance (f_0) is kept fixed at $f_0 = 4.4$ THz (left), $f_0 = 6.1$ THz (middle), and $f_0 = 8.8$ THz (right), corresponding to the middle of each avoided crossing area depicted in Fig. 5. For the case where the TINP radius is $R = 30$ nm and $R = 20$ nm, there is evidence of two distinguishable peaks forming in the spectral region of the corresponding avoided crossing points. For the case where the TINP radius is $R = 10$ nm, the two peaks are more pronounced.

with QE transition dipole moment set at $\mathbf{P} = 0.2\ e$ nm. In Fig. 5, we present the light spectra for the hybrid system under study for various TINP radii $R < 50$ nm; up to the lower threshold, the TINP model presented in Ref. [25] remains valid, ensuring that there is enough bulk material to support the surface states. We observe that the hybrid mode is blueshifted and characterized by wider avoided crossing areas, i.e., stronger coupling. Of note is the fact that no bottleneck regions are present in the spectral vicinity of the (more well-defined) avoided crossing area, hinting at the progressively diminishing effect of the zero in the absorption cross section of the TINP.

In Fig. 6, we present the light spectra for the hybrid system under study as a function of single frequency. Specifically we keep the quantum-emitter transition frequency f_0 fixed at the value corresponding to each crossing point observed in Fig. 5, and present the corresponding light spectrum as a function of incident light frequency (f). In all cases, one can observe the formation of two spectrally distinct peaks due to the coupling of the SToP polariton and the QE resonance which become more pronounced with decreasing TINP size. In Fig. 7 we extract a value for the corresponding Rabi splitting of the above cases. We note that, in an actual experiment, for this hybrid system to be in the *strong-coupling* regime, the energy separation corresponding to the avoided crossing area, the Rabi splitting, should be larger than the linewidths of the surface topological particle polariton and QE resonance states [49].

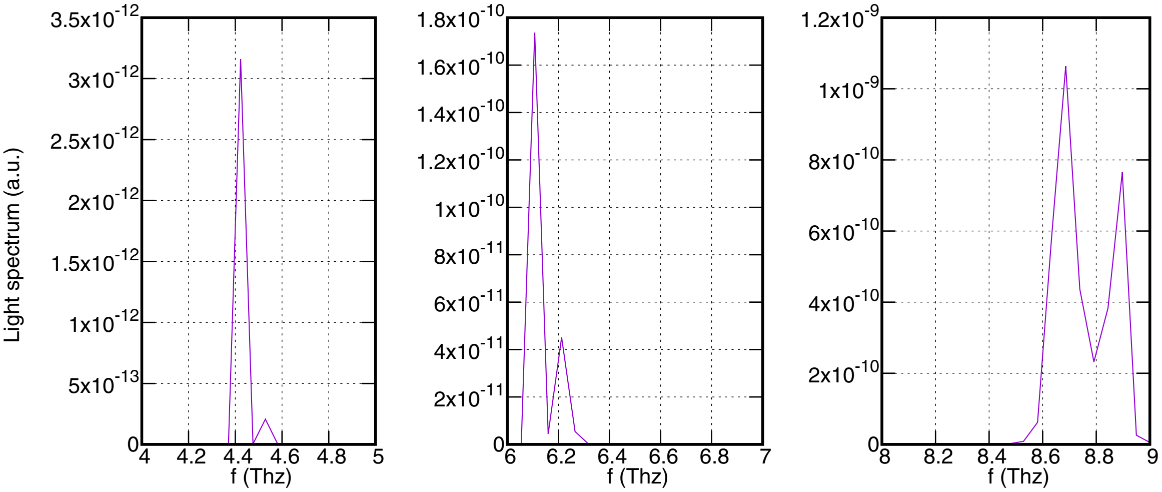

FIG. 7. Light spectra of Fig. 6 in a narrower frequency range to assess the magnitude of the Rabi splitting. A Rabi splitting of approximately $f_R \approx 0.1$ THz can be extracted for the case where the TINP radius is $R = 30$ nm (left). For a TINP radius of $R = 20$ nm (middle), the Rabi splitting is slightly larger ($f_R \approx 0.11$ THz). Finally, a larger Rabi splitting of approximately $f_R \approx 0.22$ THz is observed for the case where the TINP radius is $R = 10$ nm (right).

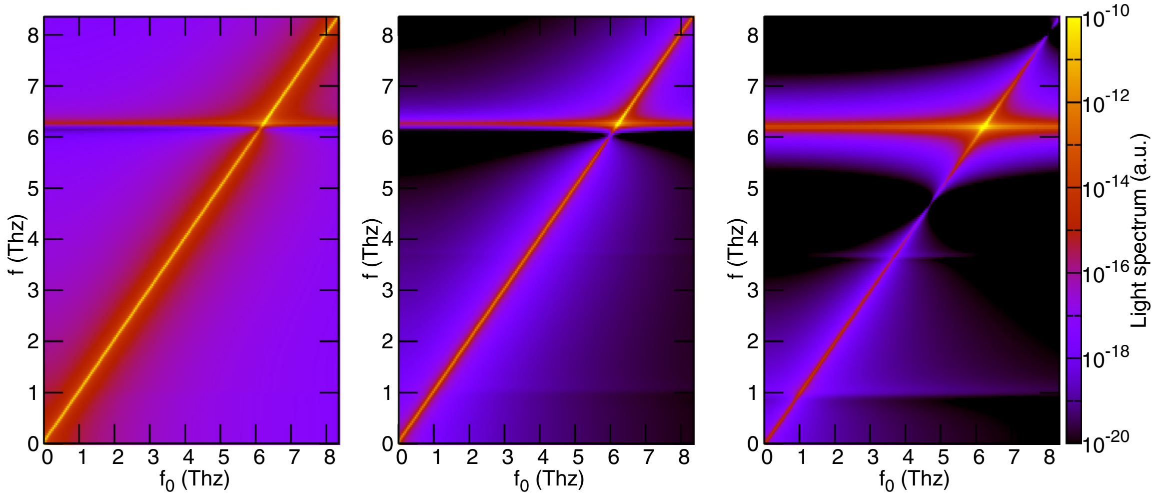

FIG. 8. Light spectra of the hybrid system under study for TINP radius $R = 20$ nm wherein the QE distance (d) from the surface of the TINP is set at $d = 10$ nm (left), $d = 5$ nm (middle), and $d = 1$ nm (right). It is evident that the SToP polariton–QE resonance coupling becomes stronger with decreasing interparticle distance.

Figure 8 illustrates the dependence of the hybrid mode with respect to the QE-TINP distance for a fixed TINP radius $R = 20$ nm. As expected, decreasing the separation between the TINP and the QE results in stronger coupling between the two, reflected in the progressively more well-defined avoided crossing area in the spectral region of the SToP mode corresponding to a TINP of the above radius.

Figure 9 presents, for completeness, the light spectra of the system under study wherein the TINP radius is set at $R > 50$ nm, illustrating the diminishing effect of the SToP mode (and by extension the hybrid mode due to the presence of the quantum emitter) with increasing TINP size, as well as an almost complete absence of the SToP mode in the case where the TINP size is tuned so that the former coincides with the bulk α phonon of Bi_2Se_3. Here, we must stress that, in all our calculations, the TINP is treated as a point dipole which is justified by the small sphere radii compared to the wavelength (the terahertz regime is an ultrasubwavelength regime for the sphere radii considered here, up to 100 nm). However, for much larger nanoparticle radii, the multiple-scattering polaritonic operator formalism employed here can readily provide a discrete dipole approximation (DDA) calculation for the TINP, as it can treat collections of an arbitrary number of point dipoles. It can thus simulate more realistically a TINP by considering it as a collection of point dipoles in the spirit of DDA. However, as explained above, due to much longer wavelength of incident radiation (terahertz regime) compared to the TINP sizes, a DDA correction would add rather unnecessary calculation complexity to our study.

We should note that the hybrid TINP-QE mode is of similar nature with respect to the modes emerging when a plasmonic nanoparticle interacts strongly with a QE [26]. However, in the case of the present work, i.e., the TINP-QE interaction, all phenomena manifest themselves much more dramatically due to the lower amount of inherent losses of the TINP in the region around the SToP resonance. This results in more pronounced peaks in the corresponding spectra, larger Rabi splittings (relative to the resonance frequency), wider

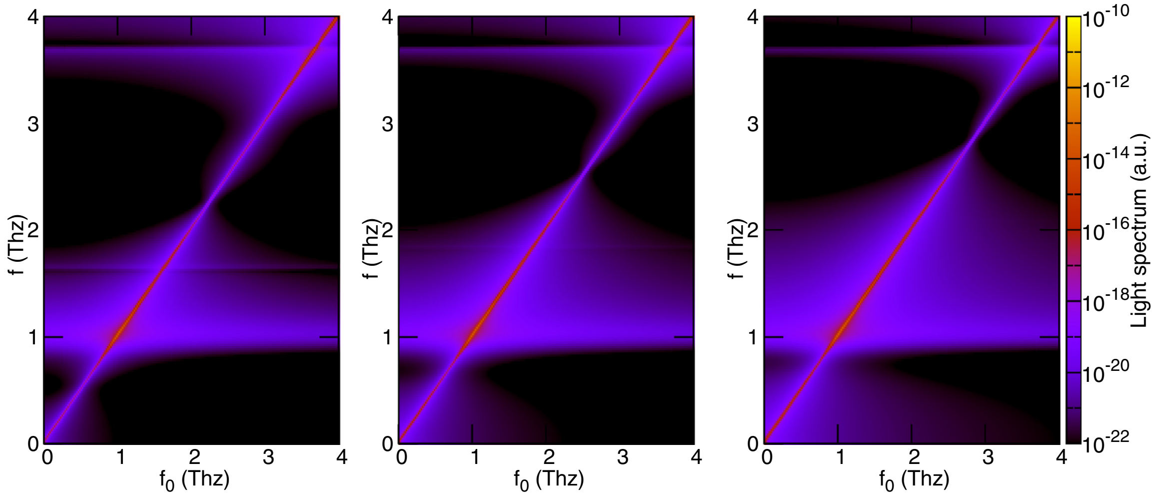

FIG. 9. Light spectra of the hybrid system under study for TINP radius $R = 90$ nm (left), $R = 80$ nm (middle), and $R = 70$ nm (right).

avoided crossing areas, etc. Moreover, the current mode lies in the terahertz regime, which is unreachable with ordinary plasmonic materials while, at the same time, allowing for easier tuning of the resonance frequency with TINP size.

Finally, a point of further investigation is the fact that the metallic surface states of the TINP are, in fact, chiral. This chirality can be taken into account in the framework of axion electrodynamics in which case the polarizability of Eqs. (2) and (3) becomes a magnetoelectric tensor [50,51]. The magnetoelectric coupling arises from the inclusion of the so-called axion (θ) term, which reflects the chirality of the surfaces states of a TI (where $\theta = \pi$). As a future work, it is worth investigating to what degree the phenomena reported here are affected by the chiral nature of the TI surface states given that magnetoelectric phenomena are, in general, second-order corrections to the EM response of materials.

IV. CONCLUSIONS

In summary, we have theoretically investigated the interaction between a spherical topological insulator nanoparticle and a single quantum emitter. Namely, we calculated the light spectrum of a single TINP-QE dimer via a previously developed method suitable to treat the interaction of light with hybrid collections of QEs and NPs [26]. The TINP was modeled via a radius-dependent correction in the ordinary insulator nanoparticle dielectric function so as to take into account the effect of the topologically protected surface states on the optical properties of the TINP [25]. We found that, under suitable conditions, the surface topological particle polariton of the former can couple strongly with the resonance state of the QE, giving rise to a previously unreported mode. Furthermore, the wavelength shift of this mode can be controlled simply via tuning the TINP size, circumventing the need to alter the surrounding dielectric material as is the norm in hybrid systems of metallic nanoparticles and quantum emitters. Investigating the conditions under which TINP-QE systems enter the strong-coupling regime should prove useful in applications to lasers, waveguides, and sensors in the terahertz range [52,53]. The case examined in the present work is the simplest one, i.e., that of a single dimer, in order to provide a first glimpse of the underlying physics of such hybrid structures before moving on to (in general, more complex) arrays of *many* TINP-QEs via methods such as the one presented in Ref. [26].

ACKNOWLEDGMENTS

G.D.C. acknowledges support by the General Secretariat for Research and Technology (GSRT) and the Hellenic Foundation for Research and Innovation (HFRI).

[1] P. W. Anderson, *Basic Notions of Condensed Matter Physics* (Westview Press, Boulder, CO, 1997).

[2] C. L. Kane and E. J. Mele, Phys. Rev. Lett. **95**, 226801 (2005).

[3] D. J. Thouless, M. Kohmoto, M. P. Nightingale, and M. den Nijs, Phys. Rev. Lett. **49**, 405 (1982).

[4] X. G. Wen, Adv. Phys. **44**, 405 (1995).

[5] J. E. Moore, Nature (London) **464**, 194 (2010).

[6] X. L. Qi and S. C. Zhang, Phys. Today **63**(1), 33 (2010).

[7] M. Z. Hasan and C. L. Kane, Rev. Mod. Phys. **82**, 3045 (2010).

[8] X.-L. Qi and S. C. Zhang, Rev. Mod. Phys. **83**, 1057 (2011).

[9] B. A. Bernevig, T. L. Hughes, and S.-C. Zhang, Science **314**, 1757 (2006).

[10] M. König, S. Wiedmann, C. Brüne, A. Roth, H. Buhmann, L. W. Molenkamp, X.-L. Qi, and C.-L. Zhang, Science **318**, 766 (2007).

[11] L. Fu and C. L. Kane, Phys. Rev. B **76**, 045302 (2007).

[12] D. Hsieh, D. Qian, L. Wray, Y. Xia, Y. S. Hor, R. J. Cava, and M. Z. Hasan, Nature (London) **452**, 970 (2008).

[13] H. Zhang, C.-X. Liu, X.-L. Qi, X. Dai, Z. Fang, and S.-C. Zhang, Nat. Phys. **5**, 438 (2009).

[14] Y. Xia, D. Qian, D. Hsieh, L. Wray, A. Pal, H. Lin, A. Bansil, D. Grauer, Y. S. Hor, R. J. Cava, and M. Z. Hasan, Nat. Phys. **5**, 398 (2009).

[15] D. Hsieh, Y. Xia, L. Wray, D. Qian, A. Pal, J. H. Dil, J. Osterwalder, F. Meier, G. Bihlmayer, C. L. Kane, Y. S. Hor, R. J. Cava, and M. Z. Hasan, Science **323**, 919 (2009).

[16] Y. L. Chen, J. G. Analytis, J.-H. Chu, Z. K. Liu, S.-K. Mo, X. L. Qi, H. J. Zhang, D. H. Lu, X. Dai, Z. Fang, S. C. Zhang, I. R. Fisher, Z. Hussain, and Z.-X. Shen, Science **325**, 178 (2009).

[17] K.-I. Imura, Y. Yoshimura, Y. Takane, and T. Fukui, Phys. Rev. B **86**, 235119 (2012).

[18] V. Parente, P. Lucignano, P. Vitale, A. Tagliacozzo, and F. Guinea, Phys. Rev. B **83**, 075424 (2011).

[19] T. Neupert, S. Rachel, R. Thomale, and M. Greiter, Phys. Rev. Lett. **115**, 017001 (2015).

[20] Y. Zhang, Y. Ran, and A. Vishwanath, Phys. Rev. B **79**, 245331 (2009).

[21] R. Egger, A. Zazunov, and A. L. Yeyati, Phys. Rev. Lett. **105**, 136403 (2010).

[22] K.-I. Imura, Y. Takane, and A. Tanaka, Phys. Rev. B **84**, 195406 (2011).

[23] F. Zhang, C. L. Kane, and E. J. Mele, Phys. Rev. B **86**, 081303(R) (2012).

[24] Y. Zhang, K. He, C. Z. Chang, C.-L. Song, L.-L. Wang, X. Chen, J.- F. Jia, Z. Fang, X. Dai, W.-Y. Shan, S.-Q. Shen, Q. Niu, X.-L. Qi, S.-C. Zhang, X.-C. Ma, and Q.-K. Xue, Nat. Phys. **6**, 584 (2010).

[25] G. Siroki, D. K. K. Lee, P. D. Haynes, and V. Giannini, Nat. Commun. **7**, 12375 (2016).

[26] G. D. Chatzidakis and V. Yannopapas, J. Mod. Opt. **65**, 951 (2018).

[27] M. Wubs, L. G. Suttorp, and A. Lagendijk, Phys. Rev. A **70**, 053823 (2004).

[28] A. Delga, J. Feist, J. Bravo-Abad, and F. J. Garcia-Vidal, Phys. Rev. Lett. **112**, 253601 (2014).

[29] P. Ben-Abdallah, S. A. Biehs, and K. Joulain, Phys. Rev. Lett. **107**, 114301 (2011).

[30] B. T. Draine, Astrophys. J. **333**, 848 (1988).

[31] O. J. F. Martin and N. B. Piller, Phys. Rev. E **58**, 3909 (1998).

[32] A. Yaghjian, Proc. IEEE **68**, 248 (1980).

[33] M. A. Yurkin and A. G. Hoekstra, J. Quant. Spectrosc. Radiat. Transfer **106**, 558 (2007).

[34] M. A. Yurkin and A. G. Hoekstra, J. Quant. Spectrosc. Radiat. Transfer **171**, 82 (2016).

[35] B. Huttner and S. M. Barnett, Phys. Rev. A **46**, 4306 (1992).

[36] H. T. Dung, L. Knöll, and D.-G. Welsch, Phys. Rev. A **62**, 053804 (2000).

[37] N. P. Butch, K. Kirshenbaum, P. Syers, A. B. Sushkov, G. S. Jenkins, H. D. Drew, and J. Paglione, Phys. Rev. B **81**, 241301(R) (2010).

[38] C.-X. Liu, X.-L. Qi, H. J. Zhang, X. Dai, Z. Fang, and S.-C. Zhang, Phys. Rev. B **82**, 045122 (2010).

[39] P. Borri, W. Langbein, S. Schneider, U. Woggon, R. L. Sellin, D. Ouyang, and D. Bimberg, Phys. Rev. Lett. **87**, 157401 (2001).

[40] S. Kako, M. Miyamura, K. Tachibana, K. Hoshino, and Y. Arakawa, Appl. Phys. Lett. **83**, 984 (2003).

[41] A. E. Schlather, N. Large, A. S. Urban, P. Nordlander, and N. J. Halas, Nano Lett. **13**, 3281 (2013).

[42] O. Pérez-González, J. Aizpurua, and N. Zabala, Opt. Express **21**, 15847 (2013).

[43] D. E. Gómez, H. Giessen, and T. J. Davis, J. Phys. Chem. C **118**, 23963 (2014).

[44] A. Trügler and U. Hohenester, Phys. Rev. B **77**, 115403 (2008).

[45] E. Waks and D. Sridharan, Phys. Rev. A **82**, 043845 (2010).

[46] C. Van Vlack, P. T. Kristensen, and S. Hughes, Phys. Rev. B **85**, 075303 (2012).

[47] M. M. Dvoynenko and J. K. Wang, Opt. Lett. **38**, 760 (2013).

[48] K. V. Nerkararyan and S. I. Bozhevolnyi, Opt. Lett. **39**, 1617 (2014).

[49] P. Torma and W. L. Barnes, Rep. Prog. Phys. **78**, 013901 (2015).

[50] A. M. Essin, J. E. Moore, and D. Vanderbilt, Phys. Rev. Lett. **102**, 146805 (2009).

[51] T. Ochiai, J. Phys. Soc. Jpn. **81**, 094401 (2012).

[52] S. Atakaramians, V. S. Afshar, T. M. Monro, and D. Abbott, Adv. Opt. Photonics **5**, 169 (2013).

[53] B. Ferguson and X. C. Zhang, Nat. Mater. **1**, 26 (2002).